Approximate velocity scale for primary and secondary dual-inlet side-dump flows [†]

Seung-chai Jung[1], Byung-Hoon Park[1], Hyun Ko[2] and Woong-sup Yoon[3,*]

[1]*The Graduate School, Department of Mechanical Engineering, Yonsei University, Seoul, 120-749, Korea*
[2]*MicroFriend Co., Ltd., Seoul, 139-743, Korea*
[3]*Department of Mechanical Engineering, Yonsei University, Seoul, 120-749, Korea*

Abstract

Effects of the bulk inlet velocity on the characteristics of dual-inlet side-dump flows are numerically investigated. Non-reacting subsonic turbulent flow is solved by a preconditioned Reynolds-averaged Navier-Stokes equation system with low-Reynolds number $k - \varepsilon$ turbulence model. The numerical method is properly validated with measured velocity distributions in the head dome and the combustor. With substantial increase in the bulk inlet velocity, general profiles of essential primary and secondary flows normalized by the bulk inlet velocity are quantitatively invariant to the changes in the bulk inlet velocity.

Keywords: Ramjet combustor; Velocity scale; Secondary flow; Turbulent mixing

---

1. Introduction

An integrated rocket-ramjet (IRR) featured by a single combustor, which commonly serves boosting and ram operations, is superior to the conventional two-combustor tandem ram jet in the aspect of the weight budget and operational complexity. Among several inlet configurations for IRR combustors, the side-dump method has been investigated as an alternative to the coaxial-dump combustor. In a side-dump combustor, the air jets projecting from multiple inlet ducts collide each other with a prescribed angle and distance at an impingement point on the axis of the combustor. Caused by the inlet jet impingement, recirculating flow, which functions as a thermal bath, is formed in the head dome cavity bounded by side-inlet imping jets and the head dome plate. Fig. 1 sketches primary and secondary
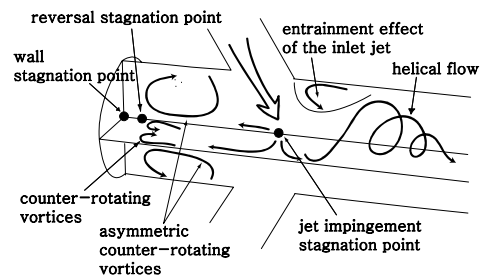

Fig. 1. Schematic of flow evolutions in dual-inlet side-dump ramjet combustor.

flows in a side-dump dual-inlet combustor; the side-inlet jet, the jet impingement, the jet-wall collision, the recirculating flow in the dome region, the helical flow, and the developing duct flow far downstream [1]. Head dome zone upstream of the jet impingement stagnation point is characterized by two asymmetric counter-rotating vortices on the vertical plane and by four counter-rotating vortices on the horizontal plane. A secondary recirculation zone is formed by the shearing effect of the inlet air at the immediate down-

---

stream of the inlet port. Strong helical flow is induced after the impingement of the two jets in a cylindrical combustor core. This helical vortex commands the air-fuel mixing downstream. The helical vortex continues to evolve into a fully developed core flow. Unlike the distinct length scale (distance of the reversal stagnation point from the inlet port) that characterizes the vortical flow motions in the head dome, the core flow shows no distinct length scale since all secondary flows terminate within a narrow region at an immediate downstream of the impinging jet stagnation point.

The IRR combustor with side-dump inlets lacks a flame holder because the internal ballistics of the solid rocket boosting may not be smooth due to the presence of the flame holder, or the flame holder situated in hot gas may be damaged. But, use of the flame holder is crucial for anchoring and stabilizing the flame, or a strongly advective air-stream may blow off the flame out. This highly inertial air-flow imposes unfavorable requirement onto ram combustion [2]. Theoretically, flame blow-off occurs when the rate of the convective species transport exceeds that of the heat transfer. In side-dump combustors, a secondary stream like slowly recirculating flow in the head dome shown in Fig. 1 is helpful to balance the heat and mass transports, and then the flame stabilization solely depends on secure supply of the activation energy. The recirculating hot gas in the head dome serves to ignite the unburned gas mixture. Specifically, due to the head dome geometry with one end enclosed by the head dome plate and the other end open to incoming airstream, the inlet jet entrains the hot gas from the head dome and the heat transported from entrained hot gas ignites the unburned gas mixture. Owing to such peculiar route of energy supply for ignition, the flame can be securely anchored. The system of vortices in the head dome cavity is crucial to the stable operation of the combustor. Suitably conditioned flow and reaction environments are essential to successive ignition and flame holding.

Because flame stabilization in a side-dump combustor heavily depends on the inlet flows, a number of studies have centered on elucidating the flow filed [3, 4]. Particularly, many experimental and analytical efforts have centered on determining an optimal dome height for the best blow-off performance [3, 5-9]. The combustor flows are distinguished by two flow regimes bifurcated at the jet-impingement stagnation point. The low speed fluids in the head dome, espe-

cially those adjacent to the head plate, play the role of a nearly stagnant wall to the upstream bifurcating flow [5]. If the dome height is equal to or greater than the radius of the cylinder, the flow field downstream of the jet-impingement stagnation point is no longer altered by the dome height [6]. The physical distance between the cross-sectional plane in the head dome and the plane passing through the upstream edge of the inlet port provides the length scale for the flows of the head dome. Ko and Yen [7] numerically showed that the flow recirculation in the head dome is either separated from the core flows or stretched out toward the entrance port as the side-inlet angle decreases.

However, compared with extensive studies on the flow field under various head dome and side-inlet geometries, researches on the effect of bulk inlet velocity are limited. Bulk inlet velocity is supposed to be an essential operational parameter affecting aerodynamic stabilization of the flame, because the collision strength between two inlet jets and the bulk velocity of the primary flow could affect formation of secondary flows, including recirculating flow in the head dome. Therefore, detailed understanding regarding the coupling mechanism between the inlet flow and the secondary flows under different inlet bulk velocity is indispensable. In the present study, the bulk inlet velocity (inlet Mach number) is examined as to whether it characterizes the head dome and the core flows and provides a velocity scale for the side-dump dual-inlet combustor flows. Numerical simulations of non-reacting turbulent combustor flows are conducted.

2. Numerical strategy and solution procedure

The flow solver is based on the conservation form of full three-dimensional Navier-Stokes equation in curvilinear coordinates. To cope with the convergence problem caused by the use of compressible flow equation for low Mach number flows, the governing equations are preconditioned by a pseudo-time preconditioner. Preconditioned Reynolds-averaged Navier-Stokes equations for conservations of mass, momentum, energy, turbulent kinetic energy and its dissipation rate can be expressed in a tensor form as follows:

$$\Gamma\frac{\partial Q_v}{\partial \tau}+\frac{\partial Q}{\partial t}+\frac{\partial F_j}{\partial x_j}+\frac{\partial G_j}{\partial x_j}=H \tag{1}$$

where

$$Q_v = \left[p', v_i, T, k, \varepsilon \right]^T$$

$$Q = \left[\rho, \rho v_i, e, \rho k, \rho \varepsilon \right]^T$$

$$F_j = \left[\rho v_j, \rho v_i v_j + p' \delta_{ij}, (e + p') v_j, \right.$$
$$\left. \rho v_j k, \rho v_j \varepsilon \right]^T$$

$$G_j = \left[0, -\tau_{ij}, -\tau_{ij} v_i + q_i, \tau_{ki}, \tau_{\varepsilon i} \right]^T \qquad (2)$$

In Eqs. (1) and (2), repeated indices imply summation in the range of the index, i, j=1, 2, 3 for three dimensions. In the momentum equation, the body force was neglected. Here, the fluid is an air, and a uniform temperature profile is assumed at the inlet boundary. A preconditioner by Venkateswaran [10] treats the convergence problem typical for low Mach number flows solved by a time marching scheme. Eigenvalues are rescaled for the convergence acceleration.

The turbulence correlation expressed by the Reynolds stresses must be modeled to close the set of equations. A two-equation turbulence model based on eddy viscosity is suitable for a CPU-effective calculation. A $k - \varepsilon$ turbulence model is easy to solve with flow equations and avoids the algebraic description of turbulent length scale, and the low Reynolds number $k - \varepsilon$ turbulence model suggested by Yang and Shih [11] was adopted. By assuming Kolmogorov timescale as the minimum for turbulence, this model avoids a singularity problem at the wall boundary. All constants appearing in the turbulence model repeat the values in the reference [11]. This simplified turbulence treatment fits well for the present problem configuration since the mixing phenomenon weakly depends on the wall turbulence.

The numerical scheme is based on the approximate factorization algorithm, which is implicit, second-order accurate, and computational- ly robust in solving the Navier-Stokes equations. In this scheme, the algebraic equation discretized by the Euler implicit method is time-integrated by LU factorization method [12, 13]. Roe's [14] flux difference splitting method was used for the discretization of inviscid flux and the flux vector splitting method by Sterger-Warming [15] for the inviscid flux jacobians. The viscous terms are discretized by central differencing method. A modified TVD scheme [16] tailored for preconditioning method was employed to ensure the numerical stability and higher-order spatial
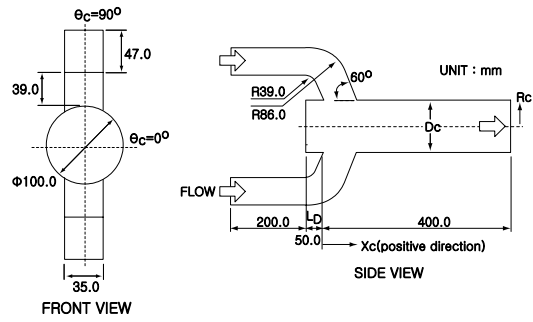

Fig. 2. Front and side view of dual-inlet side-dump ramjet combustor with sizes [5].

accuracy. For cost-effective computation, the space-decomposition parallel computation algorithm was used in conjunction with MPI (message passing interface) technique and a multiple partitioning method for an optimum load balancing.

The geometry of the dual-inlet side-dump combustor, coordinate system, and dimensions are presented in Fig. 2. For the convenience of the code validation, the geometry of the combustor repeats previous experimental study [5]. The dome height (L_D) and the combustor diameter (D_c) are 50*mm* and 100*mm*, respectively. The model combustor is equipped with two curved rectangular inlet ducts installed on a circular chamber with an inlet angle of 60°. Centerlines of two inlet ducts intersect on the cylinder center axis. Upstream edge of the inlet ports is taken as the zero-reference point for longitudinal coordinate (X_c). The flow distribution above the dump plate is neither the uniform nor the seventh power law. It is characterized by the six-vortex structure in the transverse direction and flow reversal in the streamwise direction, and resulting helical flow is dumped into the combustion chamber [5]. To mimic physical inflow condition, an inlet duct is extended to upstream of the reference point ($X_c^* = -5$). Here X_c^* ($\equiv X_c / D_c$ if X_c^* is positive and X_c / L_D if X_c^* is negative) defines dimensionless longitudinal coordinate. The cylinder length is truncated at four duct diameter where the cylinder flow is fully developed. The helical flows with their axis parallel to the center axis are generated immediately after the jet impingement point and decay rapidly. From the separate calculations, all secondary flows including the helical vortex evolve into a unilateral flow, proceed downstream, and gradually proximate to its fully developed profile after $X_c^* = 4.0$ [5, 6].
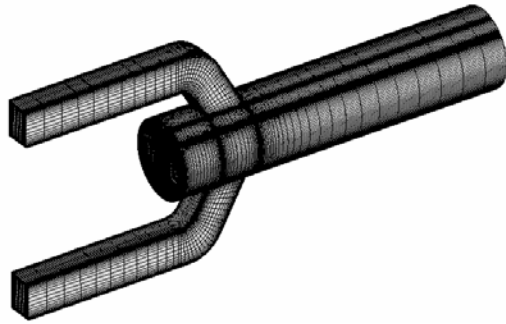
Three-dimensional rescaled hyperbolic partial

Fig. 3. Multiblock structured grid for side-dump combustor. (block 1: 60×81×69, block 2: 20×81×69, block 3: 27×27×41, block 4: 27×27×41, 506898 grid points in total).

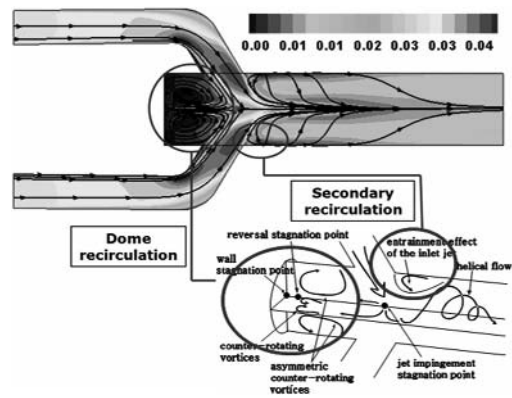Fig. 4. Mach number contours and streamlines on the cross-section at 90° plane.

Fig. 5. Stream line in the dome and secondary recirculation region.

differential equations are solved with the boundary conditions of (1) symmetric planes ($\theta_c = 0°$ and $\theta_c = 90°$), (2) axis-symmetry at the centerline ($R_c = 0$), (3) fully developed outlet boundary condition ($X_c^* = 4.0$), (4) physical inflow at the entrance of the inlet duct, and (5) no-slip conditions at all solid walls. Where, the boundary conditions of (1) and (2) are only applied to the quarterly segmented grid system. As noted in the previous studies [5-7], the ram flow exhibits unique and complex flow characteristics. Paralleled with the use of a robust high-resolution numerical method, the physical domain must be finely segmented so that the small-scale fluid motions can be resolved. Fig. 3 depicts a multiblock mesh system composed of 506898 grid points.

3. Results and discussion

Primary and secondary flows are simulated with validation, and the effect of the inlet bulk velocity is examined parametrically. In section 3.1, velocity, temperature and pressure of the inlet bulk flow are 9.907m/s, 300K, and 1atm, respectively. These flow conditions are the same with those of the previous experimental study [5]. With this inlet flow the Reynolds number based on the combustor bulk flow velocity is 2.6×10^4 and the flows are in the turbulent regime. Inlet bulk flow velocity depends on the flying speed and the structure of shock deceleration. For parametric examination of the flow field, the inlet Mach number is varied in the range from 0.1 to 0.4 in section 3.2, which corresponds to the velocity range from 34.7 m/s to 138.9 m/s. Inlet Mach numbers in this range fit into a practical design locus of the side-dump dual-inlet ramjet combustor.

3.1 General features of primary and secondary flows

A dual-inlet side dump combustor consists of three major parts of inlet duct, head dome, and combustor cylinder (Fig. 1). As was previously stated, this side-dump configuration gives rise to complex three-dimensional flows concomitant with a variety of primary and secondary flows. Fig. 4 depicts iso-Mach number and stream lines of the combustor flows on the cross-section at $\theta_c = 90°$ along the longitudinal direction (Fig. 2). As depicted in Fig. 4, symmetrically inflowing air jets collide at the jet impingement stagnation point and give rise to a pair of counter-rotating vortices in the head dome and a secondary flow recirculation near the cylinder wall at an immediate downstream of the inlet duct.

Fig. 5 shows an enlarged view of fluid-particle trajectories passing through the primary and the secondary recirculation zone in the head dome and the cylinder. Two particle trajectories passing through the
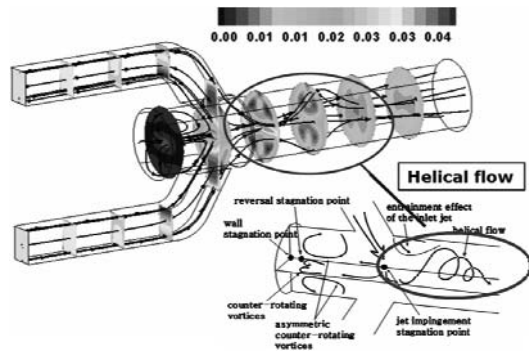
Fig. 6. Streamlines and Mach number contours at various longitudinal cross-sections.

head-dome and the secondary recirculation zones are depicted. The first stream exiting the inlet duct collides with the counter stream for symmetry, turns into and sweeps the cylinder wall, enters the secondary recirculation zone, and proceeds downstream. In contrast, the second stream entering side by side with the first fluid-particle also experiences impingement at the plane of symmetry but is entrained into the head dome. This second fluid-particle exhibits irregular vortical motions and exits from the head dome cavity, rejoins into the core flow, and eventually evolves into a helical vortex. Commanding fluid motion in the head-dome is the primary recirculation, but the fluid is circulated by a large-scale vortical motion and ventilated by fresh inlet air. This circulatory supply of the fluids which carries heat is essential to sustaining the thermal condition for continuous ignition and flame holding.

Fig. 6 portrays iso-Mach and stream lines on the cross-sectional area at eight axial locations from the inlet boundary to far downstream in the cylinder. The flow field is generally bisected into the head dome and the combustor flows. Air injected from bilateral inlet ducts is guided into the combustor and collides at the jet impingement zone located on the cylinder center line. After the impingement of the jets, fluids propagate into all directions for continuity and form a pair of counter-rotating recirculating flows in the head dome. The helical flows with their axis parallel to the central axis are also generated and rapidly settle down to the primary stream.

Fig. 7 presents the cross-sectional profile of the streamlines at three longitudinal locations in the region of head dome, jet impingement zone, and the combustor core, respectively. A helical vortex observed in Fig. 6 is projected in Fig. 7 as counter-
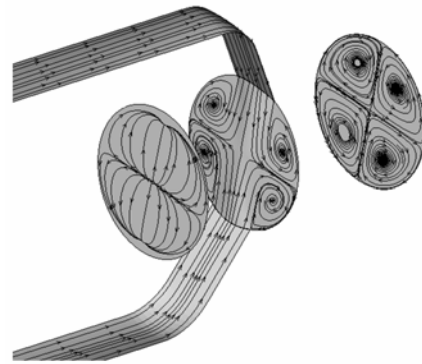

Fig. 7. Streamline on the cross-section of inlet duct, head dome, impinging region, and combustor cavity.
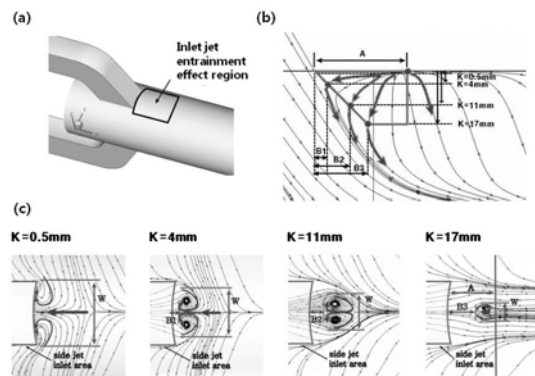

Fig. 8. Stream lines on the axial cross sections in the secondary recirculation zone.

rotating streamlines on the cross-section of the impingement zone and vortices with their axis parallel to the cylinder centerline in the combustor core. Recirculating flows in the head dome are driven by the bifurcating jet flows and the shearing inlet jets. In Fig. 7, the flow field downstream of the head dome ($X_c^* \geq 0$) appears to be symmetric with respect to the cylinder center axis. But two counter-rotating flows in the head dome ($X_c^* < 0$) show bilateral symmetry with respect to the $\theta_c = 0°$ plane. Counter-rotating low speed flow in the head dome collides with the upstream bifurcating flow at the reversal stagnation point (Fig. 1). These low speed fluids, especially those adjacent to the head plate, function as a nearly stagnant wall and limit reversing of the bifurcated stream. Strong helical vortex induced by a violent jet impingement, along with the radial flows which proportionally increase with an impingement angle, trap the fluid in the head dome cavity, entrains a part into the combustor for continuity. This unique fluid mo
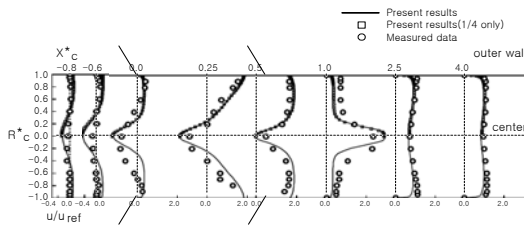
Fig. 9. Axial mean-velocity distributions in the $\theta_c = 90°$ plane.

Fig. 10. Axial mean-velocity distributions on $\theta_c = 0°$ plane.

tion impedes the smooth fluid stream while it degrades the mixing quality [7].

Fig. 8 presents planar distributions of streamlines on the cross-sections in the zone of secondary flow recirculation. As indicated in Fig. 8(a), the secondary recirculating flows anchor to the edge of the inlet port and entrain the inlet air. In Fig. 8(c), four cross-sectional streamline distributions are depicted in accordance with their vertical distances (K) from the wall of 0.5, 4, 11, and 17 mm, respectively. In Fig. 8(b), letter A is the distance from the edge of the inlet duct to the jet impingement stagnation point which is measured to be 29 mm. The counter-rotating vortex gradually shrinks and shifts downstream as the vertical distance increases. The vortex structure vanishes at the vertical distance of $K=17mm$. According to the vortex law, the vortex never ends. Hence, the angular velocity of the vortex in Fig. 8(c) rises as it stretches and conserves its angular momentum. However, as it proceeds, the primary jet and the helical vortex interrupt and hinder the vortex stretching, and this secondary vortex progressively diminishes as it stretches out. Formation of this secondary recirculation has not been reported in the previous studies.

Axial mean-velocities (solid line) are presented with measurement (hollow circles) at eight longitudinal locations in $\theta_c = 90°$ plane in Fig. 9 and $\theta_c = 0°$ plane in Fig. 10. Here, the normalized axial coordinates at eight longitudinal locations are $X_c^* = -0.8, -0.6, 0.0, 0.25, 0.5, 1.0, 2.5,$ and 4.0. Bulk combustor velocity of $u_{ref} = 4.15$ m/s sets the reference for normalizing the local velocities. In both symmetry planes, essential flow characteristics were properly predicted and velocity profiles show good agreement with the measured data obtained from the reference [5].

In Fig. 9, the inlet jets are impinged and bisected, hence the velocity vectors in the range between $X_c^* = 0.5$ and 1.0 are oppositely directed. The flows experience a sharp turn along the path lines with higher strain rate. A pair of counter-rotating flow
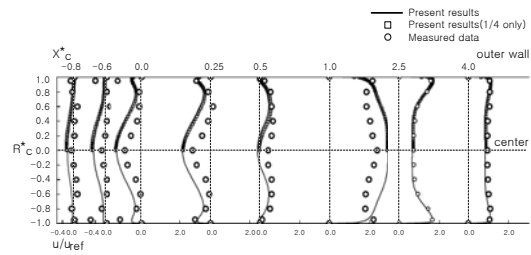
recirculations occur in the head dome ($X_c^* \leq 0$) which flows upstream along the dome centerline, turns at the head dome plate, and exits to the periphery of the wall. This counter-rotating vortical motion is sustained by the bifurcating flows projecting from the jet impingement stagnation point. It is noticed that experiments of reference [5] show two counter-rotating vortices in the head dome which are different in their sizes and profiles asymmetric with respect to the central axis. This may be caused by the vortex fluctuation. If it were the case, two counter-rotating vortices may have different size alternately. But, even if it were, the two-equation $k - \varepsilon$ model is too dissipative to capture this fluctuation and predicts symmetric vortices as in Fig. 9

In Fig. 10, a plot of axial-velocity distributions on $\theta_c = 0°$ plane is shown. Consistent with the results shown in Fig. 9 ($\theta_c = 90°$), the axial velocity along the centerline shows its negative peak in the head dome cavity ($X_c^* < 0$) and the opposite holds downstream ($X_c^* \geq 0$). At $X_c^* = 0.5$, the flow is nearly stagnant on the centerline but exits from the head dome with two positive velocity peaks at $R_c^* = \pm 0.6$. This confirms the occurrence of a bifurcation of the inlet jet at the jet impingement stagnation point on the cylinder center axis and the flow turning by low speed fluids in the head dome, which functions as a nearly stagnant wall. Due to this inlet jet bifurcation, resultant flows evolve in a distinct bimodal pattern. From $X_c^* = 0.5$ to 1.0, the axial velocity increases because the fluids spread into the side wall and rejoin the core flow. This detouring fluid motion caused by the inlet jet impingement gives rise to three-dimensional helical flows. In the short axial distance from $X_c^* = 1.0$ to 4.0, this helical vortex structure vanishes rapidly by turbulent diffusion and the axial velocity decreases along the cylinder centerline, while the core flow grows fully developed. It is noted that experimental results show, but the simulation fails to predict, a minor vortex occurring in a narrow region
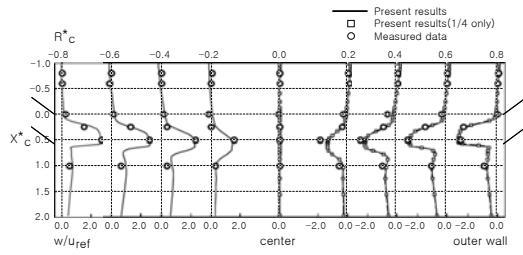
Fig. 11. Radial mean-velocity distribution in the $\theta_c = 90°$ plane.

Fig. 12. Centerline profiles of the mean axial and radial velocity components.

adjacent to the wall. The use of the $k - \varepsilon$ turbulence model provides a plausible cause for this discrepancy because the two-equation models are valid for strongly turbulent flows in which transports by the eddy diffusivity commands.

It is noted that the hollow-squares drawn in the upper half ($R_c^* \geq 0$) of Fig. 9 and 10 are the results obtained by the use of only a quarterly segmented grid system, one-fourth of the full mesh system (Fig. 3). This quarter grid system bounded by perpendicular symmetry planes at $\theta_c = 0°$ and $90°$ includes 126,724 grid points, one-fourth of the original DOFs. For cost-effective computations, the quarter grid system was repeatedly used for a parametric investigation of the effects of the inlet velocity with no loss in the solution accuracy.

Concomitant with their impingement, the jet streams are squeezed into thick bulk fluids and stretch out into the lateral direction in order to conserve their momentum. The momentum carried by the impinging jets is transported into a merged stream with new axial and lateral components. A fraction of the lateral momentum increases in proportion to an impingement angle. Fig. 11 presents profiles of radial velocities at nine radial locations in the $\theta_c = 90°$ plane. Since two impinging jets in $\theta_c = 0°$ plane are the same in their magnitude but opposite in their radial direction, the radial velocity becomes nearly zero at the cylinder centerline ($R_c^* = 0$). The jet-like mean velocity profile between $X_c^* = 0.0$ and 1.0 manifests an occurrence of the bifurcating flow projecting from the jet-on-jet impingement zone. At the location adjacent to the inlet port ($X_c^* = 0.5$, $R_c^* = \pm 0.8$), radial velocities suddenly drop because a secondary recirculation zone (Fig. 8) emerges from this zone. This secondary recirculation is driven by the shearing force exerted by the inlet jet. Due to convective (turbulent) dissipation of the helical vortex, the radial velocities progressively vanish as the flows proceed down
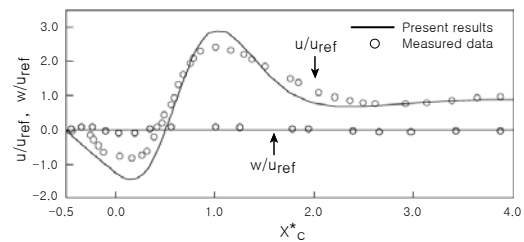
stream.

Fig. 12 plots axial and radial velocities along the combustor center axis (where the normalized axial coordinate was defined as $X_c^* = X_c / D_c$ for both positive and negative coordinate). As the flow proceeds downstream ($0.5 < X_c^* < 1.0$), the maximum axial velocity gradually shifts from the side wall toward the core region (Fig. 10) and radial velocity vanishes (Fig. 11). This flow pattern is repeatedly observed in Fig. 12. In which the axial velocity in the centerline increases in the region of $0.5 < X_c^* < 1.0$ and reaches its maximum at $X_c^* = 1.0$. As the flows proceed further downstream ($1.0 < X_c^* < 3.0$), a large portion of the axial momentum is converted into radial momentum of the helical vortex; hence the axial velocity reaches its minimum in the region of $2.0 < X_c^* < 3.0$. And then the axial velocity is unchanged at the downstream of $X_c^* = 3.0$ where the flow grows fully developed. The jet impingement stagnation point where both axial and radial velocity are zero occurs at the axial location in the vicinity of $X_c^* = 0.5$. This point delimits two separate flow regimes along the combustor centerline.

3.2 Inlet velocity as an approximate velocity scale

Effects of bulk inlet velocity on the formation of essential primary and secondary flows were parametrically examined. Throughout whole test cases, the inlet Mach number was varied in the range from 0.1 to 0.4. Fig. 13 shows iso-Mach number and stream lines in the $\theta_c = 90°$ plane. Even with substantial augmentation in the inlet Mach number, the cross-sectional views of the duct flows appear to be all similar at first glance even though upper and lower limits of the Mach numbers in each frame are not the same. All portray general features of the dual-inlet side-dump combustor flows: inlet jet impingement, primary and secondary flow recircula-
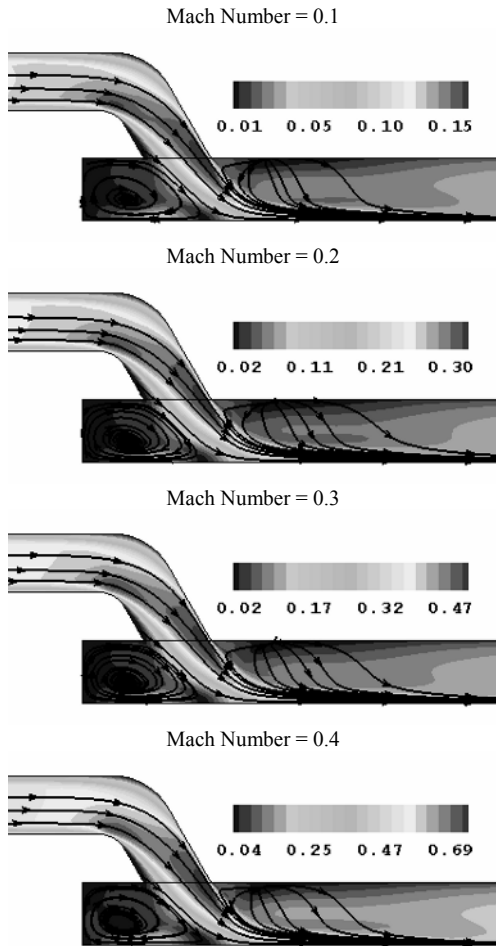
Mach Number = 0.1

Mach Number = 0.2

Mach Number = 0.3

Mach Number = 0.4

Fig. 13. Mach number contours and stream line in the $\theta_c = 90°$ plane with different inlet flow Mach number.

Mach Number = 0.1　　　　Mach Number = 0.2
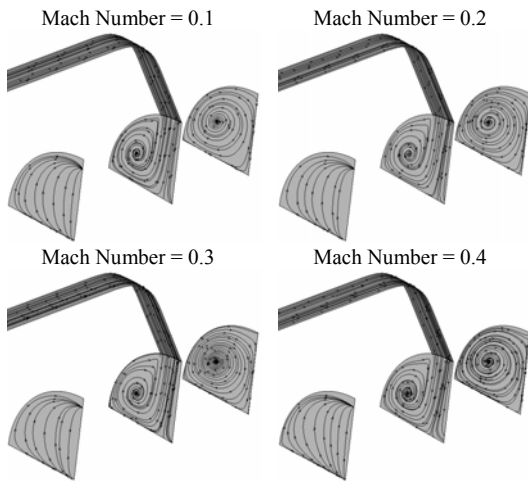

Mach Number = 0.3　　　　Mach Number = 0.4

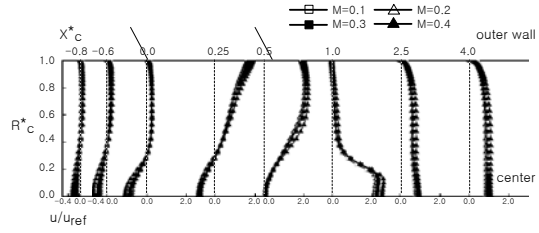Fig. 14. Stream line in the cross section with different inlet flow Mach number.

Fig. 15. Axial velocity distributions in the $\theta_c = 90°$ plane for inlet Mach number 0.1, 0.2, 0.3 and 0.4.
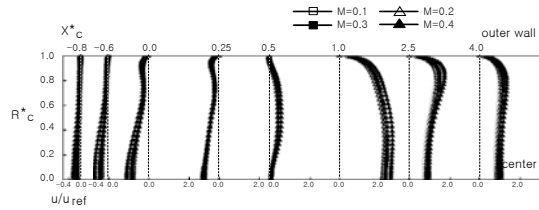

Fig. 16. Axial velocity distributions in the $\theta_c = 0°$ plane for inlet Mach number 0.1, 0.2, 0.3 and 0.4.

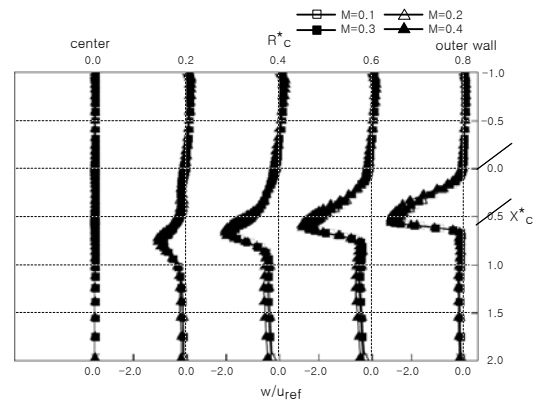Fig. 17. Radial velocity distribution in the $\theta_c = 90°$ plane for Mach number 0.1, 0.2, 0.3, and 0.4.

tions.

Fig. 14 presents planar distributions of the streamlines at three axial locations of $X_c^* = -0.8$, 0, and 0.5. Regardless of the inlet Mach number, the vortex directions are commonly clockwise, and it is qualitatively unaltered at different inlet Mach numbers. This vividly shows that large-scale rotational fluid motion is characterized by the bulk inlet velocity.

Axial mean-velocity profiles at eight longitudinal locations ($X_c^* = -0.8$, -0.6, 0.0, 0.25, 0.5, 1.0, 2.5 and 4.0) in $\theta_c = 90°$ and $\theta_c = 0°$ planes are presented in Figs. 15 and 16, respectively, which repeat those in Figs. 9 and 10. Four inlet Mach numbers were examined and resulting velocity fields were normalized by
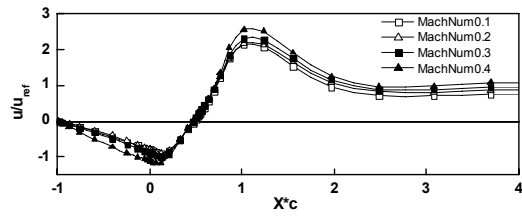
Fig. 18. Centerline profiles of the axial velocity components for Mach number 0.1, 0.2, 0.3, and 0.4.

Table 1. Entrainment ratio at different inlet Mach numbers.

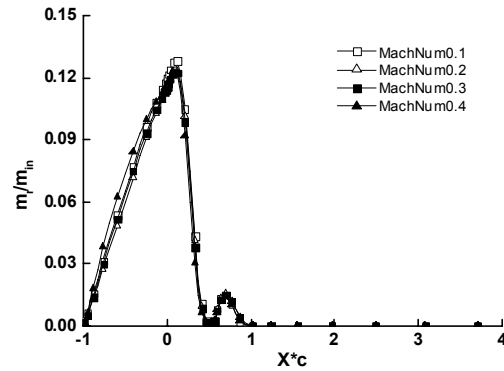| inlet Mach number	inlet bulk velocity (*m/s*)	inlet mass flow rate, $\dot{m}_{in}$ (*g/s*)	mass flow rate into the dome, $\dot{m}_r$ (*g/s*)	entrainment ratio ($\dot{m}_r / \dot{m}_{in}$)
0.1	34.7	33.96	4.01	0.118
0.2	69.4	70.54	8.01	0.114
0.3	104.2	11.42	13.01	0.114
0.4	138.9	17.74	20.46	0.115

Fig. 19. $\dot{m}_r / \dot{m}_{in}$ as a function X_c^* for inlet flow Mach number 0.1, 0.2, 0.3, and 0.4.

a half of the inlet bulk velocity at a given Mach number. All axial velocities increase in proportion to the inlet Mach number. Normalized profiles of axial velocity in both $\theta_c = 0°$ and $90°$ planes are marginally altered, and this indicates that translational fluid motion is characterized by the bulk inlet velocity.

Radial mean-velocities at five radial locations in $\theta_c = 90°$ planes are presented in Fig. 17 in terms of the inlet Mach numbers. Here, the normalized radial coordinates at five radial locations repeat those shown in Fig. 11 ($R_c^* = 0.0$, 0.2, 0.4, 0.6 and 0.8). Radial velocities were normalized by a half of inlet velocity at a given Mach number. In Fig. 17, all radial velocities increase in proportion to the inlet Mach number; however, similar to the cases for the axial velocity (Fig. 15 and 16), the profiles of normalized radial velocity are not significantly altered. Evidently, the extent of the jet penetration can be characterized by the bulk inlet velocity.

Fig. 18 plots spatial distribution of axial velocity along the combustor centerline. The jet impingement stagnation point occurs in the immediate vicinity of $X_c^* = 0.5$ at all Mach numbers, and is found to be unchanged by the inlet Mach number. This is equivalent to saying that the geometry of the dome recirculation zone is practically unaffected by the inlet flow Mach number because the dome recirculation zone is defined as a volume bounded by the head dome plate or the reversal stagnation point and the jet impingement stagnation point (Fig. 1). Thus, the recirculating flow in the head dome cavity is uniquely characterized by the bulk inlet velocity.

Since the mass fraction of the air transported into the head dome cavity ($\dot{m}_r / \dot{m}_{in}$) plays an important role in determining the extent of the recirculating flow and the flame stability, the functional dependence of $\dot{m}_r / \dot{m}_{in}$ with respect to the inlet Mach number was investigated. Fig. 19 plots local entrainment ratio (flow rate of the reversing stream normalized by that of the bulk inlet flow) at different inlet Mach

numbers. And Table 1 contains the specific values of the mass flow rate into the dome and the entrainment ratio at the entrance of the head dome ($X_c^* = 0.0$) for different inlet flow Mach numbers. With the presence of the secondary recirculation zone, the occurrence of flow reversal is evident in a narrow region between $X_c^* = 0.5$ and 0.9. It is noticed that the head vortex and the secondary recirculation zone are nearly invariant at different inlet Mach numbers. Interestingly, the entrainment ratio is insensitive to multi-fold changes in the inlet Mach number. This indicates that the mass flux through the head dome is proportionally increasing with the bulk inlet velocity, hence the flux of the activation energy.

In many applications of spray combustion, the combustion efficiency depends on the quality of the liquid vaporization and the air-fuel mixing. For typical liquid-fueled ramjet combustors, the stay time is often short to complete mixing. Thus, the ramjet combustion becomes mixing-controlled, and thus large and small-scale vortical fluid motion play a critical role for attaining higher propulsion efficiency. In IRR, the fuel may be either directly injected from the dome plate of the combustor, or laden in the ram-air and dumped into the combustor. For both cases,

the degree of the turbulent mixing determines combustion quality as a whole. Turbulence in the jet-on-jet impingement flow can be indirectly estimated by the swirl intensity and the vorticity, since large part of the turbulent kinetic energy is due to large scale swirl motion and the vorticity features the small scale fluid motion. The intensity of the swirl is defined by the swirl number, $S \equiv \int_{R_i}^{R_0} U_\theta U_x r^2 dr / \int_{R_i}^{R_0} R_0 U_x^2 r dr$ which describes the strength of the swirl motion, where U_x, U_θ, R_i, R_o and r are the axial velocity component, the tangential velocity component, the inner radius of the cylinder, the outer radius of the cylinder and the radial coordinate, respectively. Fig. 20 presents the profile of the swirl intensity along the axial direction when the inlet Mach number is 3, and Fig. 21 shows the swirl intensity normalized with respect to half of the inlet velocity for different inlet flow Mach numbers. The swirl motion is found to be most active near the inlet port ($X_c^* \approx 0.5$) and then progre-
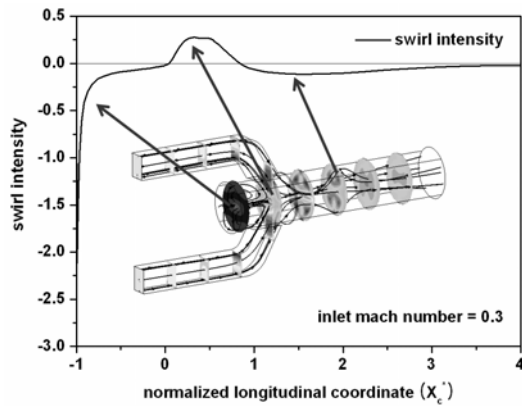
progressively diminishes. Over $X_c^* = 4$, the swirl intensity is proximate to zero. Integrated tangential velocity is counterclockwise at the cylinder downstream ($X_c^* > 1$), and thus the swirl intensity at the axial location downstream of $X_c^* > 1$ is shown to be negative. Two peaks (one positive and one negative) occur in the region of jet impingement and vortex stretching where the flows vastly change. In the regions in which a steep gradient of mean velocity causes strong turbulence, the turbulent kinetic energy reaches correspondingly higher levels. The steep gradient of the mean velocity between $X_c^* = 0.0$ and 1.0 (Fig. 17) is the source for high swirl intensity concurrent with turbulence. The profiles of normalized swirl intensity in terms of inlet flow velocity are folded into

Fig. 20. Variation of swirl intensity along the axial direction.
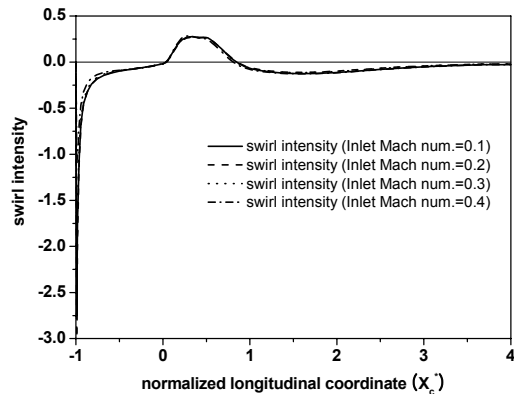
Fig. 21. Effect of the inlet Mach number on the swirl intensity.

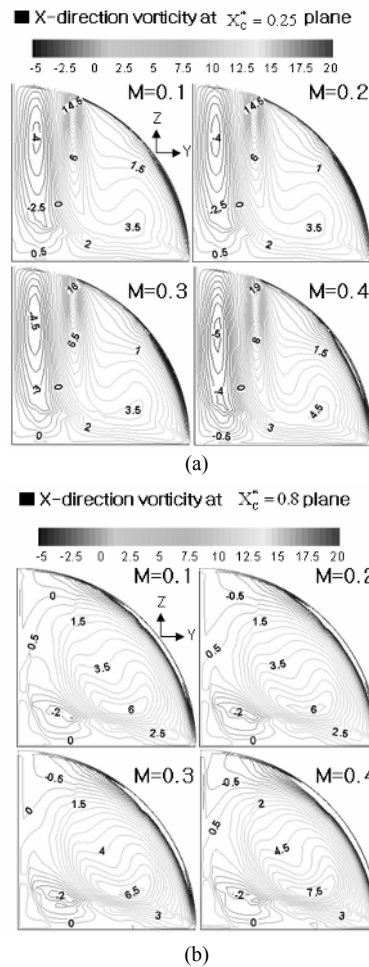
Fig. 22. Effect of the inlet Mach number on the axial vorticities (ω_x) on the cross section at (a) $X_c^* = 0.25$, and (b) $X_c^* = 0.8$. The vorticities are normalized with respect to half of the inlet velocity and the cylinder diameter.

almost a single line, and this indicates that the normalized swirl intensities are all similar. The tangential velocity of the combustor flow is thus linearly dependent on the axial velocity. It can also be deduced from Fig. 21 that the global flow structure, such as the flow recirculation, is not altered by the bulk inlet velocity because any change in flow structure alters the profile of the swirl intensity.

Fig. 22 shows the contours of axial vorticities on the cross section at two axial locations of $X_c^* = 0.25$ and $X_c^* = 0.8$. Velocity and spatial coordinates were normalized with respect to half of the inlet velocity and the combustor diameter, respectively. The mean velocity profile at $X_c^* = 0.25$ in Fig. 17 exhibits a jet-like flow which bifurcates the flows into opposite directions and shows sharp velocity gradient. This steep velocity gradient causes strong vortices in Fig. 22(a). The side-jet injected from the inlet port impacts upon the opposed jet, and after the impingement, two streams are engulfed and squeezed by the two counter-rotating vortices. Impinging opposite jets induces a pair of strong helical vortex motions symmetrically on both sides of the inlet port. In this flow situation, the fuel-rich mixture is transported toward the periphery of the combustor at the outer combustor region [7]. This fuel-rich mixture is carried into the combustor core as the two counter-rotating vortices proceed and impact upon on each other near the $\theta_c = 90°$ plane. Similar flow evolution is observed in the vorticity field. In Fig. 22(a), high-strength vorticity near inlet port is transported into the periphery of the combustor where the vorticity strength is low. This vorticity transport is primarily due to advection. As the main stream proceeds downstream, a helical vortex is formed; thus counter-clock advection transports vorticity from the periphery to the combustor core (Fig. 22(b)). From Fig. 22(a) and (b), profiles of the normalized vorticity distribution on two cross sections at $X_c^* = 0.25$ and 0.8 appear to be visually similar.

4. Conclusion

An approximate velocity scale for the dual-inlet side-dump flows was numerically investigated. Formation of the primary and secondary flows was correctly characterized with validation. Similarities in the head dome and combustor flows, inlet jet penetration, flow recirculation in the head dome, swirl intensity and vorticity due to changes in the inlet Mach number were addressed and suggest the following conclusion.

With substantial increase in the inlet Mach number from 0.1 to 0.4, general profiles of essential primary and secondary flows normalized by the bulk inlet velocity are quantitatively similar. Large scale flow structure including the jet impingement stagnation point, the size of the dome and secondary recirculation, the mass fraction of the inlet air transported to the head dome, and the distance required to settle the helical flow down to the core stream are practically invariant to the changes in the bulk inlet velocity. Axial changes in the normalized swirl intensity are identical, and the distributions of normalized vorticity are similar at all bulk inlet velocities. The bulk inlet velocity provides an approximate velocity scale for the dual-inlet side-dump flows.

Nomenclature———————————————

D_c	:	Combustor diameter
e	:	Total energy
H	:	Source term
k	:	Turbulent kinetic energy
K	:	Vertical distance from the wall
L_D	:	Dome height
M	:	Inlet Mach number
$\dot{m}_{in}$	:	Inlet flow rate
$\dot{m}_r$	:	Backward flow rate
p'	:	Perturbation pressure
q_i	:	Heat flux
R_c	:	Combustor radial coordinate
R_c^*	:	Normalized combustor radial coordinate
R_c^*	:	$2R_c / D_c$
t	:	Physical time
T	:	Temperature
u	:	Axial velocity
u_{ref}	:	Reference velocity for normalization
v_i	:	Velocity
w	:	Radial velocity
X_c	:	Combustor longitudinal coordinate
X_c^*	:	Normalized combustor longitudinal coordinate
$X_c^* \geq 0$	:	$X_c^* \equiv X_c / D_c$
$X_c^* \leq 0$	:	$X_c^* \equiv X_c / L_D$

Greek letters

Γ	:	Preconditioning matrix
δ_{ij}	:	Kronecker delta

ε	:	Turbulent dissipation rate
θ_c	:	Combustor tangential coordinate
ρ	:	Density
τ	:	Pseudo time
τ_{ij}	:	Stress tensor

References

[1] T. M. Liou *et al.*, Effects of inlet guide-vane number on flowfields in a side-dump combustor, *Experimental Thermal and Fluid Science*, 24 (2001) 11-23.

[2] Y. H. Hwang and Y. H. Hung, Turbulent transport phenomena in three-dimensional side-dump ramjet combustors, *International Journal of Heat and Mass Transfer*, 32 (1989) 2113-2125.

[3] S. P. Vanka *et al.*, Analytical. Characterization of flow fields in side inlet dump combustors, *AIAA paper*, 83-1399 (1983).

[4] F. D. Stull *et al.*, Investigation of a dual inlet side dump combustor using liquid fuel injection, *Journal of Propulsion and Power*, 1 (1985) 83-88

[5] T. M. Liou and S. M. Wu, Flow field in a dual-inlet side-dump combustor, *Journal of Propulsion and Power*, 4 (1) (1988) 53-60.

[6] T. M. Liou *et al.*, The three-dimensional jet-jet impingement flow in a closed-end cylindrical duct, *ASME Journal of Fluids Engineering*, 112 (1990) 171-178.

[7] T. H. Ko and R. H. Yen, Three-dimensional non-reacting turbulent mixing phenomena in a side-dump combustor, *Journal of CSME*, 14 (4) (1993) 350-359.

[8] P. R. Choudhury, Characterization of a side dump gas generator ramjet, *AIAA paper*, 82-1258 (1982).

[9] T. M. Liou *et al*, Prediction of confined three-dimensional impinging flows with various turbulent models, *ASME Journal of Fluids Engineering*, 114 (1992) 220-230.

[10] S. Venkateswaran and C. L. Merkle, Analysis of preconditioning methods for the Euler and Navier-Stokes equations, *Von Karman Institute Lecture Series*, 1999-03 (1999).

[11] Z. Yang and T. H. Shih, New time scale based $k-\varepsilon$ model for near-wall turbulence, *AIAA Journal*, 31 (1993) 1191-1198.

[12] A. Jameson and E. Turkel, Implicit schemes and *LU* decomposition, *Mathematics of Computation*, 37(156) (1981) 385-397.

[13] J. S. Shuen, Upwind differencing and *LU* factorization for chemical non-equilibrium Navier-Stokes equations, *Journal of Computational Physics*, 99 (1992) 233-250.

[14] P. L. Roe, Approximate Riemann solvers, parameter vectors and difference schemes, *Journal of Computational Physics*, 135 (1997) 250-258.

[15] J. L. Steger and R. F. Warming, Flux vector splitting of the inviscid gas dynamic equations with application to finite-difference methods, *Journal of Computational Physics*, 40 (1981) 263-293.

[16] S. Y. Hsieh and V. Yang, A preconditioned flux-differencing scheme for chemically reacting flows at all Mach numbers, *International Journal of Computational Fluid Dynamics,* 8 (1997) 31-49.

Seung-chai Jung received his B.S. degree in Mechanical Engineering from Yonsei University, Korea, in 2001. He then received his M.S. degree in Mechanical Engineering from Yonsei University, Korea, in 2005. Mr. Jung is currently a Ph. D. candidate at Yonsei University, where he is majoring in Mechanical Engineering. Mr. Jung's research interests include propulsion system and particle-surface collision dynamics.

Byung-Hoon Park received his B.S. degree in Mechanical Design and Production Engineering from Yonsei University in 2003. He is currently a Ph.D. candidate in Yonsei University in Seoul, Korea. His research interests include performance design of propulsion systems and nu-merical analysis of instability in multi-phase turbulent reacting flow-fields.

Hyun Ko received his B.S. degree in Aerospace Engineering from Chonbuk National University, Korea, in 1996. He then received his M.S. degree in Mechanical Design from Chonbuk National University, Korea, in 1998. In 2005, he obtained his Ph.D. degree from Yonsei University, where he majored in mechanical engineering. Dr. Ko is currently a Principal

Research Engineer of the MicroFriend Co., Ltd. in Seoul, Korea. His research interests include propulsion related systems and computational fluid dynamics.

Woong-sup Yoon received his B.S. degree in Mechanical Engineering from Yonsei University, Korea, in 1985. He then received his M.S. degree from University of Missouri-Rolla in 1989. In 1992, he obtained his Ph.D. degree from the University of Alabama in Huntsville, where he majored in mechanical and aerospace engineering. Dr. Yoon is currently a professor at the School of Mechanical Engineering at Yonsei University in Seoul, Korea. His research interests include propulsion system and particle-related environmental/thermal engineering.